LES Algorithm for Turbulent Reactive Flows Simulation

IONUT PORUMBEL, CRISTIAN CÂRLĂNESCU, FLORIN GABRIEL FLOREAN, CONSTANTIN EUSEBIU HRITCU
National Research and Development Institute for Gas Turbines COMOTI
220D, Iuliu Maniu Boluevard, sector 6, 061126, Bucharest
ROMANIA
ionut.porumbel@comoti.ro http://www.comoti.ro

Abstract: - The paper presents the development and implementation of a Large Eddy Simulation numerical algorithm for simulating turbulent reactive flows. The numerical algorithm is based on a 5 step modified Runge - Kutta numerical scheme with a dual time stepping numerical convergence acceleration technique, and employs a Localized Dynamic Turbulent Kinetic Energy turbulence model. The chemical reaction part of the algorithm is handled by a Linear Eddy Mixing combustion model. The paper described in brief the numerical algorithm, the turbulence model and the combustion model, highlighting the improvements they bring to the numerical solution in terms of accuracy and suitability to real life combustion problems. The algorithm validation is also performed, by comparison to experimental data and the literature and the superior algorithm accuracy is highlighted by comparison to numerical data resulting from previous numerical studies. The algorithm presented here is, to the knowledge of the authors, the first such complex implementation on Romania and will be used by Romanian researchers to tackle complex turbulent combustion problems with state-of-the-art methods and computational tools.

Key-Words: - Large Eddy Simulation, Linear Eddy Model, Runge - Kutta numerical scheme

1 Introduction

1.1 Previous Work

With the recent advances in the computer technology, the numerical simulations of both reactive and non-reactive flow have become ever feasible and the use of numerical simulations for research studies is becoming ever more important.

Reynolds Averaged Navier Stokes (RANS) simulations of premixed reactive flows were reported by many researchers in the field [1, 2, 3, 4, 5] with varying degrees of success. However, important discrepancies in the numerical results could not be avoided due to shortcomings stemming mostly from the RANS' inability to handle the smaller turbulent scales that are key to the combustion process.

The later development of the Large Eddy Simulation (LES) technique [6, 7, 8] allowed a significant improvement of numerical simulation accuracy in general. In LES, the three dimensional large scale motion is resolved, hence the geometry dependent flow features are captured accurately, and only the small scales that exhibit local isotropy are modeled.

Due to its ability to resolve a larger range of turbulent scales, the method is more appropriate to simulate turbulent flows. Numerical simulations of premixed reactive flows using this technique were reported in references [9-18].

Stone and Menon [19, 20] and Duwig et al. [21] conducted LES of partially premixed combustion in swirling lows using spatially and temporally variable inflow equivalence ratio. An analysis of the dynamic response of the combustor to these variations in equivalence ratio has shown that the heat release oscillations caused by the variation in the equivalence ratio can either enhance, or damp the pressure oscillations in the combustor.

A novel approach for LES of partially premixed combustion has been proposed recently [22, 23] based on the flame index approach that quantifies the occurrence in the flow of the premixed, or the non-premixed combustion regime. Other studies [24] proposed a combination of the conserved scalar approach and the G-equation model for partially premixed combustion and validated the method by simulating a bluff body stabilized flow.

Recently, numerical studies of the dynamics of the premixed bluff body stabilized flame using Lagrangian methods have been reported [25, 26, 27].

Some DNS studies have also been reported over the last years [28], but they are only limited to small domains due to the important computational cost that makes DNS prohibitive for real-life combustor numerical simulations.

1.2 Combustion and Turbulence

In most combustion related applications, the Reynolds number characteristic of the fluid flow in the flame

region is sufficiently high such that the combustion process occurs in a turbulent flow field. The effects of the turbulence are generally advantageous for the efficiency of the combustion, since turbulence enhances the mixing of component chemical species and heat [29], but adverse effects upon combustion can also occur, if the turbulence level is sufficiently high to create flame extinction. In turn, combustion may enhance the turbulence through dilatation and buoyancy effects caused by the heat release. Thus, a thorough understanding of the combustion process occurring in a combustor, for instance, would require first understanding the interplay and interdependency between combustion and turbulence. However, the field of turbulent combustion is still an open research
topic ("the most significant unresolved problem in classical physics" [29]) and significant research efforts are currently underway towards this end.

The most important theoretical issue that arises when considering turbulent combustion problems is the interdependency of the various time and length scales involved. Besides the diversity of scales brought into play by the turbulence, combustion occurs at molecular levels and involves a multitude of elementary chemical reactions, each with its own characteristic length scale. If one is to consider simultaneously the entire range of scales involved, the problem becomes a lot more complex and also, when numerical simulation is considered, more computationally expensive. Therefore, a simplifying hypothesis was sought: the so - called hypothesis of "scale separation" [29]. The hypothesis assumes that in the inertial sub-range the scales of the combustion process are separated from the scales characteristic for the turbulence. The idea behind it is that once the ignition point is reached and the chemical reaction moves on the upper branch of what the combustion literature calls "the S - shaped curve" [29] the chemical reactions are faster than any turbulent time scale and therefore the chemistry is independent of the inertial range turbulent mixing.

However appealing through its simplicity, and popular for the variety of combustion models based on it, this hypothesis does not always hold true and accurate modeling of combustion processes occurring in a real application combustor requires more sophisticated combustion models that avoid this hypothesis. The combustion model used here, the Linear Eddy Mixing model is among the very few that maintain validity over the entire range of combustion regimes and, therefore, has proven superiority in terms of numerical accuracy when compared to classical combustion models, as employed by most commercial CFD software [30].

2 Mathematical Formulation

2.1 Governing Equations

The equations governing the motion of an unsteady, compressible, reacting, multiple-species fluid, are the Navier-Stokes equations.

The fully compressible Navier-Stokes equations describing the conservation of mass, momentum, total energy and conservation of N chemical species are:

$$\begin{cases} \frac{\partial \rho}{\partial t} + \frac{\partial \rho u_i}{\partial x_i} = 0 \\ \frac{\partial \rho u_i}{\partial t} + \frac{\partial}{\partial x_j}\left[\rho u_i u_j + p\delta_{ij} - \tau_{ji}\right] = 0 \\ \frac{\partial \rho E}{\partial t} + \frac{\partial}{\partial x_i}\left[\left(\rho E + p\right)u_i + q_i - u_j\tau_{ij}\right] = 0 \\ \frac{\partial \rho Y_m}{\partial t} + \frac{\partial}{\partial x_i}\left[\rho Y_m\left(u_i + V_{i,m}\right)\right] = \dot{w}_m \text{ ,where m} = 1,\text{N} \end{cases} \quad (1)$$

In the above equations, u_i is the *i-th* velocity component, ρ is the mass density, p is the pressure, Y_m is the species mass fraction of the *m-th* species, V_{im} is the diffusion velocity of the *m-th* species in the *i-th* direction,

$$E = e + \tfrac{1}{2}(u_k u_k) \quad (2)$$

is the total energy per unit mass, and τ_{ij} is the viscous stress tensor, defined as:

$$\tau_{ij} = \mu\left(\frac{\partial u_i}{\partial x_j} + \frac{\partial u_j}{\partial x_i}\right) - \frac{2}{3}\mu\frac{\partial u_k}{\partial x_k}\delta_{ij} \quad (3)$$

where δ_{ij} is the Kronecker function.

Also, e is the internal energy per unit mass computed as:

$$e = \sum_{m=1}^{N} Y_m h_m - \frac{p}{\rho} \quad (4)$$

where h_m is the species enthalpy per unit mass given by:

$$h_m(T) = \Delta h_{f,m}^0 + \int_{T_0}^{T} c_{P,m}(T')dT' \quad (5)$$

In the above, $\Delta h_{f,m}{}^0$ is the enthalpy of formation per unit mass of the *m-th* species at the reference temperature T_0, T is the temperature, and $c_{P,m}$ is the specific heat at constant pressure for the *m-th* species.

Returning to Eq. 1, ωm is the mass reaction rate per unit volume of the m-th species:

$$\dot{\omega}_m = MW_m \sum_{k=1}^{L}\left(\nu''_{mk} - \nu'_{mk}\right)A_k T^{\alpha_k} e^{(-E_{a,k}/R_u T)}\Pi_{n=1}^{N}\left(\frac{X_m p}{R_u T}\right)^{\nu'} \quad (6)$$

where L is the number of chemical reactions of the considered mechanism and N is the number of species, MW_m is the mass fraction of the *m-th* species, ν''_{mk} and ν'_{mk} are the stoechiometric coefficients of the *m-th* species and for the *k-th* chemical reaction on the product and reactant side, respectively. A_k, α_k and $E_{a,k}$ are the Arrhenius rate pre-exponential coefficient, temperature exponent and activation energy for the *k-th* chemical reaction, respectively, T is the temperature and R_u is the

universal gas constant. X_m is the molar fraction of the *m-th* species.

The heat flux vector in Eq. 1 contains the thermal conduction (I), enthalpy diffusion (i.e. diffusion of heat due to species diffusion) (II), the Dufour heat flux and the radiation heat flux. Dufour heat flux and radiation heat flux are neglected [30], therefore:

$$q_i = \underbrace{-\kappa\frac{\partial T}{\partial x_i}}_{(I)} + \underbrace{\rho\sum_{m=1}^{N} h_m Y_m V_{im}}_{(II)} \quad (7)$$

where the mixture averaged thermal conductivity is:

$$\kappa = \overline{c}_P \mu / Pr \quad (8)$$

the mixture averaged specific heat at constant pressure is:

$$\overline{c}_P = \sum_{m=1}^{N} Y_m c_{P,m} \quad (9)$$

and *Pr* is the mixture Prandtl number.

The pressure p is directly derived from the equation of state for perfect gas:

$$p = \rho RT = \rho\frac{R_u}{MW_{mix}}T = \rho R_u T\sum_{m=1}^{N}\frac{Y_m}{MW_m} \quad (10)$$

Fick's Law is used to determine the species diffusion velocity:

$$V_{im} = -\frac{D_m}{Y_m}\frac{\partial Y_m}{\partial xi} \quad (11)$$

where D_m is the *m-th* species molecular diffusion coefficient. Gradients of temperature and pressure can also produce species diffusion [30] (Soret and Dufour effects, respectively) but these two contributions are neglected hereafter.

The viscosity is determined using Sutherland's law:

$$\frac{\mu}{\mu^0} = \frac{\frac{T}{T^0}^{3/2}}{\frac{T_S+T}{T^0}} \quad (12)$$

where μ^0 is the reference viscosity at temperature T^0 and $T_S = 110{,}4\ K$.

Finally, total mass conservation is ensured by enforcing:

$$\sum_{m=1}^{N} Y_m = 1 \quad (13)$$

$$\sum_{m=1}^{N} V_{im} = 0 \quad (14)$$

2.2 LES Formulation

The earliest application of the Large Eddy Simulation (LES) methodology was performed by Smagorinsky [31] and important further developments of the method were introduced later [31, 32, 33, 34].

LES resolves both the large, geometry dependent turbulent scales and a fraction of the smaller energy containing scales within the inertial range, up to a level dictated by the resolution of the numerical grid, and only the remaining scales are modeled. If the grid resolution is appropriately chosen, the unresolved scales, by Kolmogorov's hypothesis [35] are isotropic and, therefore, more amenable to modeling. This approach not only provides a lot more information but since the energy contained in the unresolved scales is much less than in the RANS approach, is also less sensitive to modeling hypotheses.

The separation between the large (resolved) and the small (modeled) scales is determined by the grid size Δ. Therefore, the Navier-Stokes equations have to be filtered with respect to the grid size in order to obtain the LES governing equations. A Favre spatial top-hat filter is employed to derive the LES equations. More details regarding the LES filtering and the different techniques are given by Ghosal [36] and Pope [37].

By applying the above mentioned filtering process to Eq. 1, the LES filtered Navier-Stokes equations can be written as [33]:

$$\begin{cases} \frac{\partial\overline{\rho}}{\partial t} + \frac{\partial\overline{\rho}\widetilde{u}_i}{\partial x_i} = 0 \\ \frac{\partial\overline{\rho}\widetilde{u}_i}{\partial t} + \frac{\partial}{\partial x_j}\left[\overline{\rho}\widetilde{u}_i\widetilde{u}_j + \overline{p}\delta_{ij} - \overline{\tau_{ij}} + \tau_{ij}^{sgs}\right] = 0 \\ \frac{\partial\overline{\rho}\widetilde{E}}{\partial t} + \frac{\partial}{\partial x_i}\left[\left(\overline{\rho}\widetilde{E} + \overline{p}\right)\widetilde{u}_i + \overline{q_i} - \widetilde{u}_j\overline{\tau_{ji}} + H_i^{sgs} + \sigma_i^{sgs}\right] = 0 \\ \frac{\partial\overline{\rho}\widetilde{Y_m}}{\partial t} + \frac{\partial}{\partial x_i}\left[\overline{\rho}\widetilde{Y_m}\widetilde{u}_i + \overline{\rho D_m}\frac{\partial\widetilde{Y_m}}{\partial x_i} + \Phi_{i,m}^{sgs} + \Theta_{i,m}^{sgs}\right] = \overline{\rho}\widetilde{\dot{w}}_m\ , \end{cases} \quad (15)$$

In the above, the over-bar denotes the spatial filtering and the ~ symbol denotes the Favre filtering.

If, in the following, k^{sgs} is the sub-grid turbulent kinetic energy, defined as:

$$k^{sgs} = \frac{1}{2}\left(\widetilde{u_k u_k} - \widetilde{u_k}\widetilde{u_k}\right) \quad (16)$$

the LES filtered total energy per unit mass can be written as [30]:

$$\widetilde{E} = \widetilde{e} + \frac{1}{2}\left(\widetilde{u}_k\widetilde{u}_k\right) + k^{sgs} \quad (17)$$

the LES filtered viscous stress tensor can be written as [30]:

$$\overline{\tau}_{ij} = \mu\left(\frac{\partial\widetilde{u}_i}{\partial x_j} + \frac{\partial\widetilde{u}_j}{\partial x_i}\right) - \frac{2}{3}\mu\frac{\partial\widetilde{u_k}}{\partial x_k}\delta ij \quad (18)$$

and the filtered heat flux as [30]:

$$\overline{q_i} = -\overline{\kappa}\frac{\partial\widetilde{T}}{\partial x_i} + \overline{\rho}\sum_{m=1}^{N}\widetilde{h_m}\widetilde{Y_m}\widetilde{V_{im}} + \sum_{m=1}^{N} q_{im}^{sgs} \quad (19)$$

where the diffusion velocities are computed using the resolved gradient of the species mass fraction and q_{im}^{sgs} represents the heat transfer via turbulent convection of species.

Finally, the equation of state can be written in a filtered form as in terms of filtered velocities and temperature as:

$$p = \rho R_u \sum_{m=1}^{N} \frac{\widetilde{Y_k}\widetilde{T}}{MW_m} + \Upsilon^{sgs} \quad (20)$$

The LES filtered equations (15) - (20) contain unresolved terms representing the effects of the unresolved scales on the resolved motion, resulting from the filtering process and denoted by the superscript *sgs*.

Summarizing, the unclosed terms that need to be modeled are: the sub-grid kinetic energy, k^{sgs}, the shear stress tensor, τ_{ij}^{sgs}, the sub-grid enthalpy flux, H_i^{sgs}, the sub-grid viscous work, σ_i^{sgs} , the sub-grid convective mass flux, $\Phi_{j,m}^{sgs}$, the sub-grid diffusive mass flux, $\Theta_{j,m}^{sgs}$, the sub-grid heat flux, $q_{i,m}^{sgs}$, the sub-grid temperature - species correlation term, Y^{sgs} and the filtered reaction rate, $\widetilde{\dot{w}}_m$

2.3 Turbulence model

The turbulence model, used to close the unresolved terms mentioned earlier, is a non - equilibrium model based on the sub-grid kinetic energy transport equation, initially developed by Schumann [38] and later improved by other researchers [39, 40, 41]. The model assumes isotropic turbulence at the sub-grid scales and tracks the sub-grid kinetic energy (k^{sgs}) using a formally derived transport equation, equation solved along with the rest of the LES equations:

$$\frac{\partial \overline{\rho} k^{sgs}}{\partial t} + \underbrace{\frac{\partial}{\partial x_i}\left(\overline{\rho}\widetilde{u}_i k^{sgs}\right)}_{I} = -\underbrace{\frac{\partial}{\partial x_i}\left(\widetilde{\rho k u_i} - \overline{\rho}\widetilde{k}\widetilde{u}_i\right)}_{II} - \underbrace{\left(\overline{u_i \frac{\partial p}{\partial x_i}} - \widetilde{u}_i \frac{\partial \overline{p}}{\partial x_i}\right)}_{III} - \underbrace{\left(\widetilde{u_i \frac{\partial \tau_{ij}}{\partial x_i}} - \widetilde{u}_i \frac{\partial \overline{\tau_{ij}}}{\partial x_i}\right)}_{IV} + \underbrace{\frac{\partial}{\partial x_i}\left(\widetilde{u}_j \tau_{ij}^{sgs}\right)}_{V} - \underbrace{\tau_{ij}^{sgs} \frac{\partial \widetilde{u}_j}{\partial x_i}}_{VI} \quad (21)$$

where:

$$k = 1/2\widetilde{u_k u_k} \quad (22)$$

In Eq. 24, term (I) represents the resolved convection, terms (II) and (III) the sub-grid turbulent convection, term (IV) is the sum of the sub-grid stress work (IV_1) and the turbulent kinetic energy dissipation (D^{sgs}), term (V) represents the sub-grid transport of turbulent kinetic energy and (VI) the turbulent kinetic energy production (P^{sgs}). Terms (II) to (VI) require closure.

The three sub-grid turbulent convection terms (II), (III) and the sub-grid stress work (IV_1) are modeled together as:

$$\mathrm{II} + \mathrm{III} + \mathrm{IV}_1 \approx -\frac{\partial}{\partial x_i}\left[\overline{\rho}\frac{(\nu + \nu_t)}{\sigma_k}\frac{\partial k^{sgs}}{\partial x_i}\right] \quad (23)$$

Here, σ_k is a constant assumed to be unity [42].

The production of sub-grid turbulent kinetic energy (P^{sgs}) can be expressed in terms of the sub-grid stress tensor:

$$P^{sgs} = -\tau_{ij}^{sgs}\frac{\partial \widetilde{u}_i}{\partial \widetilde{x}_j} \quad (24)$$

Finally, the dissipation of sub-grid turbulent kinetic energy (D^{sgs}) is modeled as:

$$D^{sgs} = C_\epsilon \overline{\rho}\frac{\sqrt{(k^{sgs})^3}}{\overline{\Delta}} \quad (25)$$

Once the sub-grid kinetic energy is known from solving Eq. 21, the sub-grid length scale is given by the filter size, Δ, the velocity scale, V^{sgs} is determined from k^{sgs} and the eddy viscosity is modeled as:

$$\nu_t = C_\nu \sqrt{k^{sgs}}\Delta \quad (26)$$

The sub-grid stress tensor τ_{ij}^{sgs}, is then closed using the sub-grid eddy viscosity and a gradient diffusion model at the grid cutoff scale:

$$\tau_{ij}^{sgs} = -2\overline{\rho}\nu_t\left(\widetilde{S_{ij}} - \frac{1}{3}\widetilde{S_{kk}}\delta_{ij}\right) + \frac{2}{3}\overline{\rho}k^{sgs}\delta_{ij} \quad (27)$$

where the resolved strain rate is defined as:

$$\widetilde{S_{ij}} = 1/2(\partial\widetilde{u}_i/\partial x_j + \partial\widetilde{u}_j/\partial x_i) \quad (28)$$

It is important to note that even though the sub-grid stress tensor model employs a gradient diffusion assumption, the large scale counter-gradient effects are accounted for, since the large scales are resolved.

The sub-grid enthalpy flux H_i^{sgs}, is also modeled using a gradient assumption and the eddy viscosity given by Eq. 26:

$$H_i^{sgs} = -\overline{\rho}\frac{\nu_t}{Pr_t}\frac{\partial \widetilde{H}}{\partial x_i} \quad (29)$$

where Pr_t is the turbulent Prandtl number, and the total enthalpy is given by:

$$\widetilde{H} = \widetilde{h} + \widetilde{u}_i\widetilde{u}_i/2 + k^{sgs} \quad (30)$$

The turbulent Prandtl number is assumed in this study as unity, following earlier studies [30], but it is important to note that Pr_t can actually be dynamically computed based on the eddy viscosity and the thermal diffusivity.

In Eq. 30, $\widetilde{h}$ is the specific mixture enthalpy.

It was proved earlier [43, 44] that the sub-grid temperature - species correlation term, Y^{sgs} can be neglected for low heat release cases but may become important otherwise. However, due to significant modeling difficulties it will henceforth be neglected. Also, the sub-grid work, σ_i^{sgs}, is neglected here, as in earlier studies [30].

Finally, closures for the filtered reaction rate, for the sub-grid convective and diffusive species fluxes, and the sub-grid heat flux will be given by the combustion model, to be described in the next subsection.

In the previous equations there are two model coefficients C_ε in Eq. 25 and C_ν in Eq. 26 that are obtained dynamically as a part of the solution, using a method called the "Localized Dynamic Kinetic energy Model (LDKM) [45, 46].

The LDKM model assumes that the resolved and the unresolved small scales behave in a similar manner and, thus, the model coefficients can be computed using similarity relationships. First, a test-filter, operating in a region close to the cutoff scale, at the small, but still

resolved, scales is defined. Usually, the size of the test-filter is twice the LES resolution. Since the turbulent quantities are known at the test-filter level, the LES model coefficients can be determined by comparing quantities resolved at the two filter scales. For details on the LDKM model, see the cited work and also reference [30].

LDKM is locally stable in both space and time without smoothing. and its advantage consists in the fact that no spatial averages are required, which makes the model easy to implement in complex geometries. Past studies [47, 48], and commercial code evaluations [49] has demonstrated the reliability and accuracy of the LDKM closure.

2.4 Combustion model

2.4.1 Governing equations

To close the remaining terms mentioned earlier, a more comprehensive closure of the scalar mixing and combustion, based on the Linear Eddy Mixing (LEM) model proposed by Kerstein [50] and developed later into a sub-grid model [50], is used.

LEM is a stochastic approach aimed at simulating, rather than modeling the effects of turbulence on the chemistry, and it is not limited by the scale separation hypothesis, discussed earlier [29]. The parameters controlling the LEM turbulent mixing model require only the validity of the Reynolds number independence of free shear flows in the limit of large Reynolds numbers, which is a safe assumption for any flow of engineering interest [29]. Due to this extended validity range, the LEM model can be expected to perform well in any combustion regime, and to be able to accurately handle flames near to, or even outside, the flammability limits.

In LEM, the scalar equations are not filtered, and instead the large scale advection, turbulent mixing by eddies smaller than the grid size, molecular diffusion and chemical reaction are resolved at their appropriate length and time scales inside each LES cell. While the LES filtered conservation equations for mass, momentum and energy are numerically integrated on the LES grid, the evolution of the species fields is tracked using a two-scale, two-time numerical approach.

For any scalar an exact and unfiltered Eulerian transport equation can be written as:

$$\rho\frac{\partial\psi}{\partial t} = -\rho u_i\frac{\partial\psi}{\partial x_i} - \frac{\partial}{\partial x_i}\Big(-\rho D_\psi\frac{\partial\psi}{\partial x_i}\Big) + \dot{\omega}_\psi \quad (31)$$

where the first right hand side term represents the total convection, the second is the molecular diffusion (D_ψ is the species dependent diffusion coefficient) and the last term is the unfiltered chemical reaction source term. The velocity vector can be decomposed into:

$$u_i = \underbrace{\widetilde{u}_i}_{I} + \underbrace{\left(u_i''\right)^{face}}_{II} + \underbrace{\left(u_i''\right)^{LEM}}_{III} \quad (32)$$

where term (I) represents the LES resolved velocity, term (II) is the sub-grid velocity at the interface between LES cells determined using the known sub-grid kinetic energy, and term (III) is the small scale velocity fluctuation inside the LEM domain, unresolved at the LES level. By using Eq. 32 and regrouping the terms in Eq. 31, equations characterizing the large (Eq. 33), respectively small scale processes (Eq. 34) can be written:

$$\rho\frac{\psi^* - \psi^n}{\Delta t_{LES}} + \rho\widetilde{u}_i\frac{\partial\psi^n}{\partial x_i} + \rho\left(u_i''\right)^{face}\frac{\partial\psi^n}{\partial x_i} = 0 \quad (33)$$

$$\psi^{n+1} = \psi^* + \int_t^{t+\Delta_{LES}} -\frac{1}{\rho}\left[\rho\left(u_i''\right)^{LEM}\frac{\partial\psi^n}{\partial x_i} - \frac{\partial}{\partial x_i}\left(\rho D_\psi\frac{\partial\psi^n}{\partial x_i}\right) - \dot{\omega}_\psi\right]dt \quad (34)$$

In the above, Δt_{LES} is the LES time step, ψ^n and ψ^{n+1} are consecutive time values of the scalar ψ evolution, and ψ^* is an intermediate solution, after the large scale convection is completed. In Eq. 34, the first term under the integral represents the sub-grid stirring, the second is the sub-grid molecular diffusion and the last accounts for the reaction kinetics.

2.4.2 The small scale processes

Molecular diffusion and chemical reaction contribution to the small scale transport are resolved on a one-dimensional grid inside each LES cell at a resolution much finer than the LES resolution, and approaching the Kolmogorov scale. The one-dimensional computational domain is aligned in the direction of the flame normal inside each LES cell, ensuring an accurate representation of flame normal scalar gradients [50]. On this domain (denoted the LEM domain hereafter) molecular diffusion (term A below), chemical reactions (term B), diffusion of heat via species molecular diffusion (term C), heat diffusion (term D) and chemical reaction heat release (term E) are resolved, according to the equations below, written for the chemical species mass fractions (Eq. 35), respectively for the temperature (Eq. 36):

$$\rho^{LEM}\frac{\partial Y_m^{LEM}}{\partial t} + F_m^{stir} + \underbrace{\frac{\partial}{\partial s}\Big(-\rho^{LEM}D_m\frac{\partial Y_m^{LEM}}{\partial s}\Big)}_{A} = \underbrace{\dot{w}_m W_m}_{B} \quad (35)$$

$$\rho^{LEM}c_P\frac{\partial T^{LEM}}{\partial t} + F_T^{stir} \underbrace{-\sum_{k=1}^{N}\rho c_{p,m}D_m\Big(\frac{\partial Y_m^{LEM}}{\partial s}\Big)\Big(\frac{\partial T^{LEM}}{\partial s}\Big)}_{C} - \underbrace{-\frac{\partial}{\partial s}\Big(\overline{\kappa}\frac{\partial T^{LEM}}{\partial s}\Big)}_{D} = \underbrace{-\sum_{m=1}^{N}h_m\dot{w}_m W_m}_{E} \quad (36)$$

Here, the superscript LEM indicates values at the sub-grid LEM level, and *s* is the spatial coordinate along the LEM domain. F_m^{stir} and F_T^{stir} represent, respectively the effect of the sub-grid turbulence on the species *m* mass fraction field and on the temperature field.

The chemical reaction rates are given using a chemical reaction mechanism for the problem at hand. For the case of the numerical simulation presented herein, a 5-species, 1-step, reduced chemical mechanism for propane / air combustion was used. The chemical equation describing the mechanism is:

$$C_3H_8 + 5O_2 \Longleftrightarrow 3CO_2 + 4H_2O \tag{37}$$

with a reaction rate given by [52]

$$\widetilde{\dot{\omega}_c} = \frac{\nu_m W_m}{\overline{\rho}} A_k exp\Big(-\frac{E_a}{R_{u,cgs}\widetilde{T}}\Big)[C_3H_8]^{c_1}[O_2]^{c_2} \tag{38}$$

where ν_m is the stoechiometric coefficient, *Ak* is a pre-exponential factor equal to *8,6 x 10*^{11}, E_a is the activation energy, equal to *3,0 x 10*^{4} calories / g, $R_{u,cgs}$ is the universal gas constant expressed in calories / gram Kelvin, *[X]* represents the molar concentration of species *X*, in moles / cm^3, and c_1 and c_2 are two coefficients, set to *0,1*, respectively *1,65* for this case [52].

The current implementation assumes a calorically perfect gas, and the sub-grid pressure, p^{LEM} is assumed constant over the LEM domain, and equal to the LES grid value, *p*, which is a valid assumption in the absence of strong pressure gradients [53].

Hence, the sub-grid density is computed from the equation of state at the sub-grid level:

$$p^{LEM} = \rho^{LEM} T^{LEM} \sum_{k=1}^{N} Y_k^{LEM} \frac{R_u}{W_k} \tag{39}$$

Radiation effects are neglected. The small-scale turbulent stirring (F_m^{stir} and F_T^{stir}) is implemented explicitly on the same grid using stochastic rearrangement events that mimic the action of an eddy upon the scalar field using a method known as triplet mapping and designed to recover the 3D inertial range scaling laws [54]. Details on the triple mapping method are given elsewhere [30], and its effect on the scalar field is illustrated in Fig. 1.

The location of this stirring event is chosen from a uniform distribution. The frequency at which stirring events occur is given by [50]:

$$\lambda = \frac{54}{5}\frac{\nu Re_{\overline{\Delta}}}{C_\lambda \overline{\Delta}^3}\frac{[(\overline{\Delta}/\eta)^{5/3} - 1]}{[1 - (\eta/\overline{\Delta})^{4/3}]} \tag{40}$$

where C_λ stands for the scalar turbulent diffusivity, set to *0,0675* [55].

The eddy size, l, ranges from the Kolmogorov scale, η, to the grid size, Δ with a distribution given by [50]:

$$f(l) = \frac{(5/3)l^{-8/3}}{\eta^{-5/3} - \overline{\Delta}^{-5/3}} \tag{41}$$

where the Kolmogorov scale is determined as:

$$\eta = N_\eta \overline{\Delta} Re_{\overline{\Delta}}^{-4/3} \tag{42}$$

and N_η is an empirical constant that reduces the effective range of scales between the integral length scale and ´ but without altering the turbulent diffusivity [54]. The value used for this study is *5* [54].

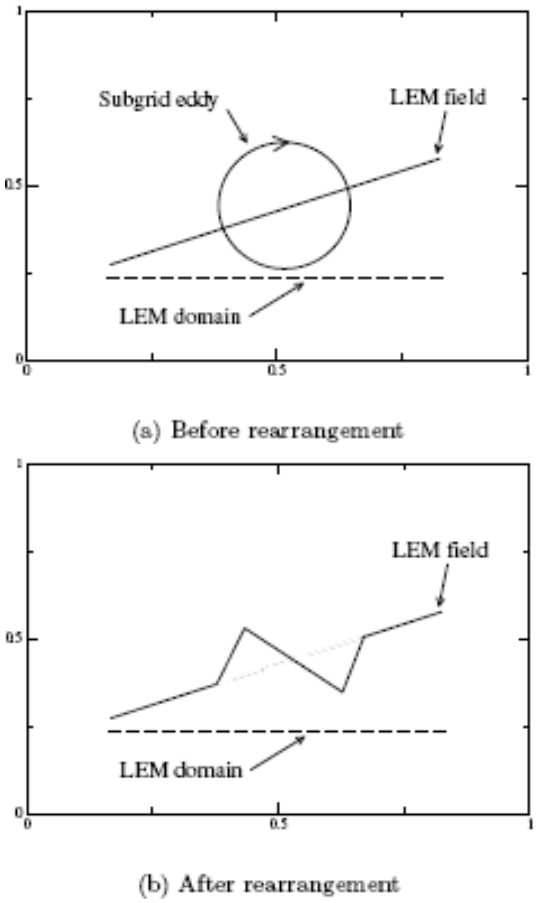

Fig. 1 - Schematic representation of the triplet mapping

2.4.3 The large scale processes

Eq. 33 is modeled using a Lagrangian transport of the scalar field across the LES cells that ensures exact mass conservation and called splicing [53]. Thus, once the LES computations are completed at a given time step, LEM domain cells (and / or cell fractions) are exchanged between the LES cells in a manner that accounts for the mass fluxes across the LES cell faces. Thus, LEM cells are transferred between the LES volumes accounting for the mass fluxes through the LES cell faces. The order in which the cell transfer on each of the spatial directions is performed is dictated by the magnitude of the mass flux in the respective direction at the resolved level [56, 57]. Next, the number of LEM cells containing the mass flux to be transported to the adjacent cell is determined. If a fractional number is obtained, the LEM cell is split so that exact mass conservation is achieved.

The sufficiently small LES time step ensures that scalars are transported from one LES cell only to an adjacent LES cell, thus drastically reducing the complexity of the problem.

2.4.4 The thermal expansion

Since the pressure in the LEM domain is assumed constant and there is no pressure gradient term in Eq. 35 or Eq. 36, the volumetric expansion of the LEM cell needs to be modeled separately, after each diffusion step, to account for the increase in volume through thermally generated pressure waves. This is done by changing the LEM cell volume according to the equation [57]:

$$\Delta V_i^{n+1} = \frac{\rho_i^n}{\rho_i^{n+1}} \tag{43}$$

where n and $n + 1$ are two consecutive diffusion steps.

Both the thermal expansion and the splicing procedure cause the LEM linear grids to be neither uniform, nor have the same number of cells in different LES cells. However, the triplet mapping procedure and the discretization method used to integrate the reaction diffusion equation require an uniform grid and a variable number of LEM cells in the computational domain will increase unnecessarily the complexity of the parallel numerical algorithm. Hence, a re-gridding procedure aimed at producing uniform grids with equal numbers of cells is applied [57].

2.4.5 The large - scale / small scale - coupling

The coupling between the large scales resolved in the LES formulation and the small scales modeled by LEM is achieved in two ways. First, the LEM model implementation uses the super-grid pressure, sub-grid kinetic energy (modeled based on super-grid quantities) and super-grid convection velocities.

On the other hand, the LEM model provides to the super-grid level Favre averaged (over the LES cell) values of species mass fractions. Based on those mass fractions, the super-grid temperature is computed. The sub-grid scalar fields in each LES cell are ensemble averaged to obtain the LES-resolved scalar field which are used in the LES energy equation and equation of state.

3 Numerical Implementation

3.1 The finite volume formulation

The LES filtered Navier - Stokes differential equations (Eq. 15) together with the sub-grid kinetic energy transport equation (Eq. 21) are solved using a finite volume 5 stages modified Runge - Kutta scheme. For this, the computational domain is divided into small volumes using a Cartesian grid and the conservation equations (Eq. 18 and Eq. 21) are applied to these control in an integral form:

$$\frac{\partial}{\partial t}\int_V \mathbf{Q}dV + \oint_S (\mathbf{F}dS_x + \mathbf{G}dS_y + \mathbf{H}dS_z) = \int_V \Phi dV \tag{44}$$

where V is the control volume delimited by surface S.

Here, $\boldsymbol{Q}$ is the state vector:

$$\mathbf{Q} = \begin{Bmatrix} \overline{\rho} \\ \overline{\rho\widetilde{u}} \\ \overline{\rho\widetilde{v}} \\ \overline{\rho\widetilde{w}} \\ \overline{\rho\widetilde{E}} \\ \overline{\rho k^{sgs}} \\ \overline{\rho\widetilde{Y_m}} \end{Bmatrix} \tag{45}$$

$\boldsymbol{F}$, $\boldsymbol{G}$, $\boldsymbol{H}$ are the fluxes on the three spatial directions, x, y and z, composed of an inviscid part, a viscous part and a sub-grid contribution:

$$\begin{cases} \mathbf{F} = F_i + F_v + F_s \\ \mathbf{G} = G_i + G_v + G_s \\ \mathbf{H} = H_i + H_v + H_s \end{cases} \tag{46}$$

In the above, the inviscid fluxes are defined as:

$$F_i = \begin{Bmatrix} \overline{\rho\widetilde{u}} \\ \overline{\rho\widetilde{u}\widetilde{u}} + \overline{p} \\ \overline{\rho\widetilde{u}\widetilde{v}} \\ \overline{\rho\widetilde{u}\widetilde{w}} \\ \overline{\rho\widetilde{u}}(\widetilde{E} + \overline{p}) \\ \overline{\rho\widetilde{u}k^{sgs}} \\ \overline{\rho\widetilde{u}}\widetilde{A} \end{Bmatrix} G_i = \begin{Bmatrix} \overline{\rho\widetilde{v}} \\ \overline{\rho\widetilde{u}\widetilde{v}} \\ \overline{\rho\widetilde{v}\widetilde{v}} + \overline{p} \\ \overline{\rho\widetilde{v}\widetilde{w}} \\ \overline{\rho\widetilde{v}}(\widetilde{E} + \overline{p}) \\ \overline{\rho\widetilde{v}k^{sgs}} \\ \overline{\rho\widetilde{v}}\widetilde{A} \end{Bmatrix} H_i = \begin{Bmatrix} \overline{\rho\widetilde{w}} \\ \overline{\rho\widetilde{u}\widetilde{w}} \\ \overline{\rho\widetilde{v}\widetilde{w}} \\ \overline{\rho\widetilde{w}\widetilde{w}} + \overline{p} \\ \overline{\rho\widetilde{w}}(\widetilde{E} + \overline{p}) \\ \overline{\rho\widetilde{w}k^{sgs}} \\ \overline{\rho\widetilde{w}}\widetilde{A} \end{Bmatrix} \tag{47}$$

The viscous fluxes are:

$$F_v = \begin{Bmatrix} 0 \\ \overline{\tau}_{xx} \\ \overline{\tau}_{xy} \\ \overline{\tau}_{xz} \\ \widetilde{u}\overline{\tau}_{xx} + \widetilde{v}\overline{\tau}_{xy} + \widetilde{w}\overline{\tau}_{xz} - \overline{q}_x \\ 0 \\ \overline{\rho} D_m \frac{\partial \widetilde{Y_m}}{\partial x} \end{Bmatrix}$$

$$G_v = \begin{Bmatrix} 0 \\ \overline{\tau}_{yx} \\ \overline{\tau}_{yy} \\ \overline{\tau}_{yz} \\ \widetilde{u}\overline{\tau}_{yx} + \widetilde{v}\overline{\tau}_{yy} + \widetilde{w}\overline{\tau}_{yz} - \overline{q}_y \\ 0 \\ \overline{\rho} D_m \frac{\partial \widetilde{Y_m}}{\partial y} \end{Bmatrix} \quad (48)$$

$$H_v = \begin{Bmatrix} 0 \\ \overline{\tau}_{zx} \\ \overline{\tau}_{zy} \\ \overline{\tau}_{zz} \\ \widetilde{u}\overline{\tau}_{zx} + \widetilde{v}\overline{\tau}_{zy} + \widetilde{w}\overline{\tau}_{zz} - \overline{q}_z \\ 0 \\ \overline{\rho} D_m \frac{\partial \widetilde{Y_m}}{\partial z} \end{Bmatrix}$$

The sub-grid contributions to the fluxes are:

$$F_s = \begin{Bmatrix} 0 \\ \tau_{xx}^{sgs} \\ \tau_{xy}^{sgs} \\ \tau_{xz}^{sgs} \\ H_x^{sgs} \\ K_x^{sgs} \\ Y_{x,m}^{sgs} \end{Bmatrix} G_s = \begin{Bmatrix} 0 \\ \tau_{yx}^{sgs} \\ \tau_{yy}^{sgs} \\ \tau_{yz}^{sgs} \\ H_y^{sgs} \\ K_y^{sgs} \\ Y_{y,m}^{sgs} \end{Bmatrix} H_s = \begin{Bmatrix} 0 \\ \tau_{zx}^{sgs} \\ \tau_{zy}^{sgs} \\ \tau_{zz}^{sgs} \\ H_z^{sgs} \\ K_z^{sgs} \\ Y_{z,m}^{sgs} \end{Bmatrix} \quad (49)$$

Finally, the source terms in Eq. (43) are:

$$\Phi = \begin{Bmatrix} 0 \\ 0 \\ 0 \\ 0 \\ 0 \\ P^{sgs} - D^{sgs} \\ \widetilde{\omega_A} \end{Bmatrix} \quad (50)$$

3.2 The Runge - Kutta scheme

Eqs. (44) are solved using a cell centered, second order discretization on a multi-block grid, using a numerical algorithm based on a 5 stage modified Runge - Kutta scheme with artificial dissipation [58, 59, 60] that allows for a higher numerical stability at larger CFL numbers, thus reducing the solution time.

Usually, Runge - Kutta schemes are employed for solving Ordinary Differential Equations (ODE), but they can also be applied to Partial Differential Equations (PDE) [61] by converting them into so called pseudo - ODEs. This achieved by separating out the partial derivative with respect to time and placing the remaining of the equation into a term that depends upon the dependent variable [62]:

$$\frac{\partial \alpha}{\partial t} = R(\alpha) \quad (51)$$

where α is any dependent variable.

Thus, once the time differencing on the left hand side of Eq. 51 is completed, the partial differential contained in the right hand side term can also be spatially differenced and any ODE integration scheme, including Runge - Kutta, is now applicable.

Generally, the modified *m* stages Runge - Kutta scheme can be formulated as:

$$\begin{aligned} Q^{(0)} &= Q^n \\ Q^{(k)} &= Q^{(0)} - \alpha_k \Delta t R^* (Q^{(k-1)}) \\ Q^{n+1} &= Q^{(m)} \end{aligned} \quad (52)$$

where *n* and *n + 1* are two consecutive time steps, *k* is the current Runge - Kutta stage, $\boldsymbol{Q}$ is the state vector, α_k are the Runge - Kutta scheme coefficients, for the case of a 5 stage scheme defined, in turn, as: 1/4; 1/6; 3/8; 1/2; 1 and $R^*(\boldsymbol{Q})$ is the residual term that includes the contribution from Euler, viscous and sub-grid fluxes and the source terms.

To eliminate spurious fluctuations of the state vector, second and fourth order artificial dissipation terms, based on pressure switches are added to the residual term [58, 63]:

$$\widetilde{D}(Q^k) = \beta_k D(Q^k) + (1 - \beta_k) D(Q^{k-1}) \quad (53)$$

such that the new residual terms become now:

$$R_e(Q^k) = R(Q^k) + \widetilde{D}(Q^k) \quad (54)$$

In Eq. 53, the coefficients β_k are set to 1.0; 0.0; 0.56; 0.0; 0.44 for maximum numerical stability.

3.3 The dual time stepping method

The advance of the numerical solution in time can be achieved numerically in two generic ways: implicit or explicit. Explicit schemes use information at a given time *t* to compute the new value of the different variables at time $t+\Delta t$. On the other hand, implicit schemes use the information at time $t + \Delta t$ to compute the value of the different variables at time $t + \Delta t$.

The explicit method has the advantage of simplicity in implementation but it has significant numerical stability constraints, usually requiring times steps smaller than the physically achievable ones. Reversely, implicit methods are less constrained by numerical stability but are far more difficult to implement, especially in parallel algorithms. Jameson [64] proposed a method combining the advantages of the afore mentioned approaches,

known as the dual time stepping approach. The governing equations are discretized implicitly with a second order backwards equation:

$$\frac{\partial \vec{Q}}{\partial \tau} + \frac{3\vec{Q}^{n+1} - 4\vec{Q}^{n} + \vec{Q}^{n-1}}{2\Delta t} + \vec{R}(\vec{Q}^{n+1}) = 0 \quad (55)$$

The above mentioned approach also implemented in the algorithm described here, was to consider the second and third terms in the Eq. 55 as the total residual of the state vector on a fictitious pseudo time τ:

$$\frac{\partial \vec{Q}}{\partial \tau} = \vec{R}^{*}(Q) \quad (56)$$

where

$$\vec{R}^{*}(Q) = \frac{3\vec{Q}^{n+1} - 4\vec{Q}^{n} + \vec{Q}^{n-1}}{2\Delta t} + \vec{R}(\vec{Q}^{n+1}) \quad (57)$$

Thus, by solving Eq. 56 with a standard explicit method and using the maximum locally available time step until convergence to the steady state is iteratively achieved, the solution of Eq. 55 can also be advanced in time with a much larger time step. Specifically, it has been observed that in regions where momentum is close to zero the convergence of Eq. 55 is significantly delayed compared to the rest of the computational domain. In order to avoid an important increase in computation time with only marginal improvements in the accuracy of the solution, the maximum number of iterations performed in solving Eq. 55 is limited to 250 after which convergence is declared. Obviously,
this introduces some inaccuracy in the solution, but it impacts strongly on reducing the computation time.

3.4 The LEM implementation

The first requirement for the numerical implementation of LEM is the numerical integration of the reaction diffusion Eq. 35 or 36. Previous studies [57] have shown that implicit schemes are very expensive in terms of memory requirements, so an explicit method is used in this study. The method uses an operator splitting technique [54, 65] based upon a sequential application of individual operators describing different physical phenomena, each at the appropriate time scale.
In the reaction - diffusion Eq. 35 - 36, four distinct phenomena are identifiable, therefore four separate time scales:

3.4.1. Molecular diffusion timescale

The time scale is associated to species and temperature transport by diffusion and is the largest timescale involved [57]:

$$\Delta t_{diffusion} = \kappa \frac{\Delta s^2}{\max(D_k)} \quad (58)$$

where Δs is the LEM grid size, D_k is the diffusion coefficient of species k and κ is a model constant, set here to 0:25 for reasons of numerical stability [57].

3.4.2 Chemistry timescale

This time scale, Δt_{chem}, is associated to the chemical reaction rates and it is usually the smallest time scale [57]. Its value is determined by the stiffness of the chemical reaction rates equation system. The implementation in the current study uses a chemical time step 10 times smaller than the molecular diffusion time scale, $\Delta t_{diffusion}$.

3.4.3 Thermal expansion timescale

The time scale is associated with the volumetric expansion induced by the increase in temperature through chemical heat release. In the current implementation it is assumed that, in the fast chemistry limit, the heat release is controlled by the molecular mixing [57], therefore:

$$\Delta t_{expansion} = \Delta t_{diffusion} \quad (59)$$

3.4.4 Turbulent stirring timescale

The time scale is associated to the turbulent convection by small (sub-grid) eddies and is defined by:

$$\tau_{stir}(x) = \frac{1}{\lambda \overline{\Delta}} \quad (60)$$

where λ is the turbulent stirring frequency, given by Eq. 40.

3.4.4 The operator splitting method

To explicitly solve all these processes appropriately, an operator splitting method [66, 67] is used. This technique allows for decoupled time resolution of the chemical, diffusion and turbulent processes. Thus, at each LES time step the diffusion and stirring time scales are determined. The chemical species source terms are determined and integrated over the diffusion time step. With this term known, the reaction - diffusion equation, less the turbulent stirring contribution is integrated at the diffusion time step. After each integration time step, thermal expansion is implemented as described earlier. At a frequency given by Eq. 40, the integration process in interrupted by the triplet map rearrangement of the scalar fields simulating the turbulent eddy.
From a numerical standpoint, the LEM domain resolution is a function of the LES resolution and the turbulence intensity. The length of the LEM domain, L^{LEM} is defined as:

$$L^{LEM} = \frac{\Delta V_{LES}^{\frac{1}{3}}}{N^{LEM}} \quad (61)$$

where N^{LEM} is the number of LEM cells per LES cell and ΔV^{LES} is the volume of the LES cell. For the triplet mapping algorithm to work, the resolution on the LEM domain has to be uniform and the number of LEM grid

points has to at least 6 and a multiple of 3. The value used for this study is 12.

3.4.5 The splicing algorithm

After the sub-grid algorithm is completed at each LES time step and for each LES cell, a Lagrangian advection of the scalar LEM fields is performed using the LES resolved velocities. The splicing species transport between adjacent LES domains is achieved by the algorithm that splices the species field successively in the three spatial directions:

The splicing is done once in every spatial direction and is performed using an upwind scheme. The absolute value and the sign of the filtered momentum term determines the order in which splicing is performed. The largest negative flux will be the first one to exit the LES cell, while the largest positive flux will be the last one to enter the LES cell.

The effect of the splicing algorithm in a 2-D representation is presented in Fig.2. Further details on the splicing numerical procedure are given elsewhere [57].

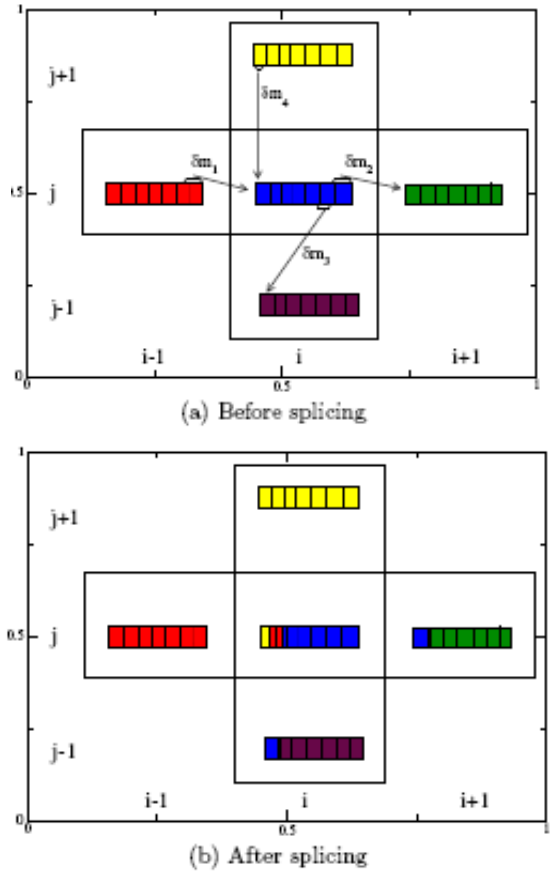

Fig. 2 - Schematic representation of the triplet mapping

Finally the re-gridding procedure presented earlier is carried out to ensure uniform LEM grid resolution and constant number of LEM cells in all LES cells.

4 Validation Results and Discussion

4.1 Numerical setup

The validation numerical simulations presented here where performed in a geometry that reproduces a previous experimental study the Volvo experiment [68] and consists of a rectangular duct of size *1.0 m x 0.24 m x 0.12 m* with a triangular prism that extends between the two lateral walls of the combustor, as shown in Fig. 3. The side of the bluff body triangular base, *a*, measures *0.04 m*.

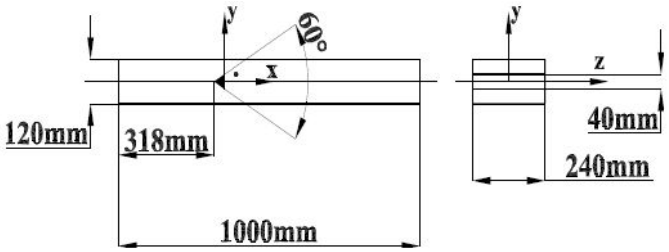

Fig. 3 - Schematic of the validation geometry

The computational domain was divided into 10 blocks, and each block was discretized by a body fitting grid with dimensions given in Table 1 and positioned according to Fig. 4.

Block	i	j	k
1	45	52	90
2	35	52	90
3	278	52	90
4	90	52	90
5	278	81	90
6	90	81	90
7	45	52	90
8	35	52	90
9	278	52	90
10	90	52	90

Table 1 - Computational grid dimensions

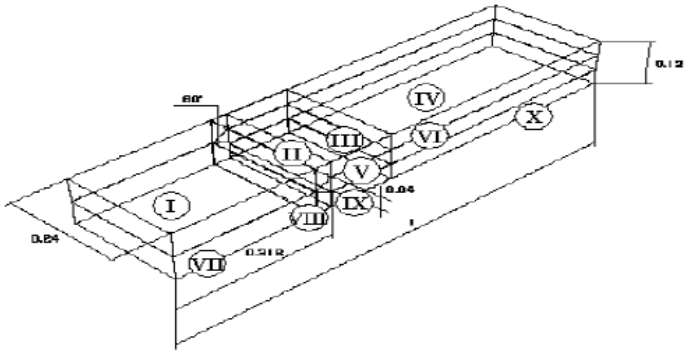

Fig. 4 - Spatial disposition of the computational blocks

The computational grid is stretched both axially and transversally and provides the maximum resolution in the two separated shear layers, immediately downstream of the bluff body, resolved by about 20 grid points. The

grid stretching is maintained under 5 percent for reasons of numerical stability.

For the LEMLES, 12 LEM cells are used in each LES cell. Using the predicted k^{sgs} and the local Δ, the maximum local sub-grid Re_Δ is *130* and $\eta = 25 \times 10^{-6}$ m. Thus, scales down to about 3η are resolved in the sub-grid. Due to heat release, the local Re_Δ in most of the grid will be lower than this value and hence, the sub-grid resolution is considered acceptable.

The inflow velocity is 17:3 m/s with a 2 percent turbulence intensity under standard atmospheric conditions. The reference Reynolds number based on inflow velocity and bluff body height is *45500*. The inflow consists of a propane - air mixture of *0.65* equivalence ratio. The simulations are carried out for five flow-through times before the flow statistics are collected, and the time averaged data presented herein are collected over a period equal to five flow-through times.

4.2 Time averaged results

This section will presents the time averaged results of the validation numerical simulation denoted LEMLES, compared to experimental data in the literature [68]. Results of an earlier numerical simulation of the same geometry using an Eddy Break - Up [69] combustion model are also included, for comparison, and denoted EBU.

Figure 5 presents the normalized axial velocity profile along the combustor centerline, behind the bluff body

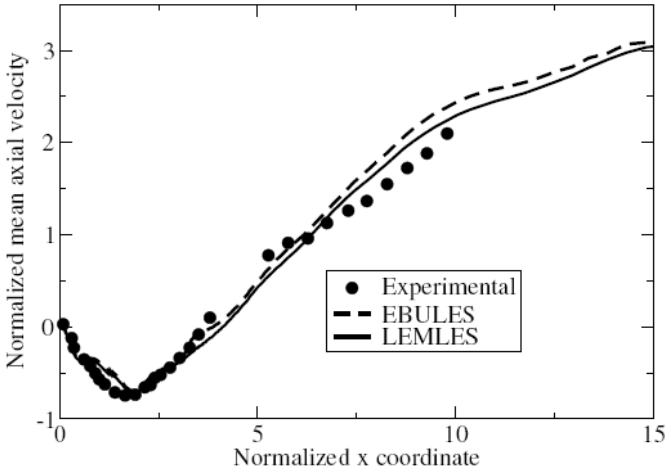

Fig. 5 - Centerline variation of the normalized time-averaged axial velocity. The velocity is normalized by the inflow value, and the distance is normalized by the bluff body size, *a*.

The numerical result matches closely the experimental data. Immediately downstream of the bluff body, the velocity is negative and reaches a negative maximum of about 0,75 of the inflow velocity at about twice the size of the bluff body, in agreement with the experimental data The length of the recirculation region is about 3.75 a. After the end of the reverse flow zone, the mean axial velocity increases upstream to gradually approach an outflow velocity about three times larger than the inflow velocity, due to the addition of chemical energy through combustion.

Both numerical studies using two different combustion models yield equally accurate results, although the current study appears to show slightly better agreement, which is due to a better temperature prediction in the far field, as it will be shown later.

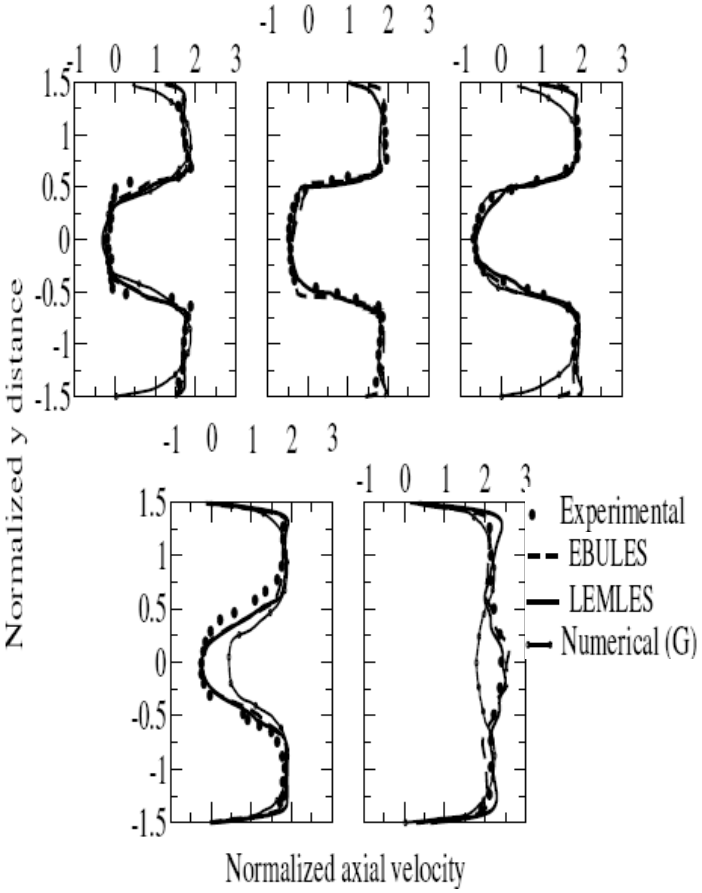

Fig. 6 – Transverse profiles of the normalized time-averaged axial velocity, at the normalized axial locations, from left to right: *0.375 a, 0.95 a, 1.53 a, 3.75 a* and *9.4 a*. The velocity is normalized by the inflow value, and the distance is normalized by the bluff body size, *a*.

In the transverse direction, the accuracy of the current numerical simulation results is also acceptable, as seen in Fig. 6. In addition to the experimental and numerical results mentioned earlier, a third set of numerical data pertaining to another previous study [18], marked by letter G in Fig. 6 and using an Eddy Dissipation Model (EDM) is also shown for comparison, The numerical accuracy of the current study is not significantly improved in this case when compared to the earlier work, except that the current study predicts a more accurate axial velocity in the free stream, correlating

well with the improved temperature predictions, to be shown later. Also, far downstream, the centerline velocity becomes over-predicted by the EBU models, indicating that the predicted acceleration rate is slightly off.

In the case of the transverse component of the time-averaged velocity, the agreement with the experimental [68] is generally good, as shown in Fig. 7.

The large scale vortical structures, created by the presence of the bluff body, decrease in intensity with the distance from the obstruction, as the wake momentum deficit diminishes and the flow tends to recover its initial axial direction. The maximum transverse velocity is about 30% of the inflow velocity, and is achieved at about 0.4 a. A notable feature of the flow field is the sudden decrease of the transverse velocity at the flame front. This behavior correlates with the pair of stationary, counter-rotating vortices that form at the sharp edge of the bluff body in the case of a reacting flow around it. The effect disappears further downstream, where the intensity and the coherence of the vortices weaken.

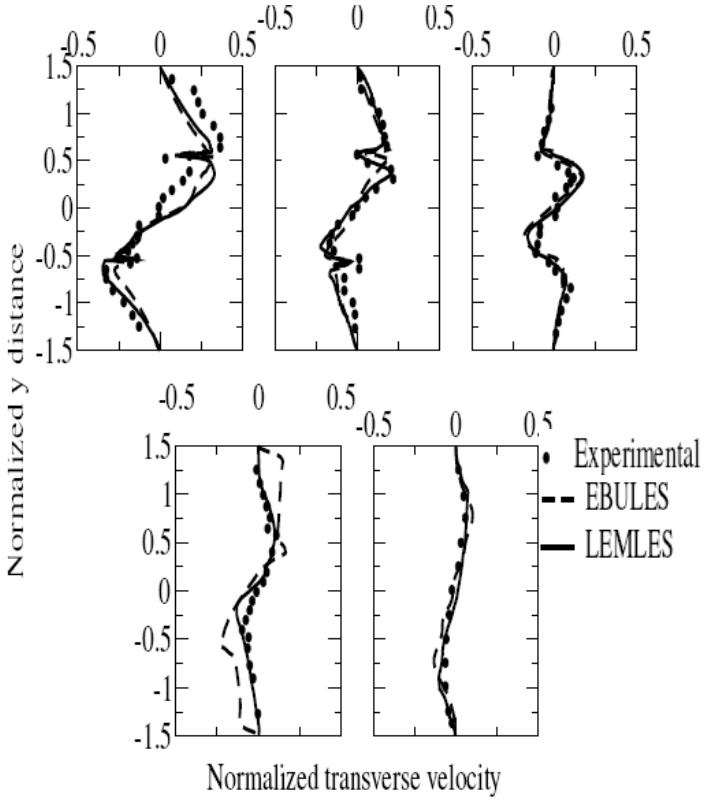

Fig. 7 – Transverse profiles of the normalized time-averaged transverse velocity, at the normalized axial locations, from left to right: *0.375 a, 0.95 a, 1.53 a, 3.75 a* and *9.4 a*. The velocity is normalized by the inflow value, and the distance is normalized by the bluff body size, a.

Overall, even if from a validation standpoint the numerical results obtained by using the algorithm presented herein are excellent, these results appear to suggest only modest improvements when using the LEM combustion model. However, the improvements do appear in regions where mixing between the products and the reactants is occurring and where the flame structure exists. This subtle fact becomes clearer when the time-averaged temperature profiles are compared in Fig. 8. As earlier, the numerical data reported by Giacomazzi et al. [18] is shown for comparison

It can be seen that the earlier EBU study under-predicts the mean temperature in the centerline region. As a consequence, the flame thickness is overestimated by EBU as well [30] and the EBU flame is slower to respond to the turbulent fluctuations, and the intermittency effect is not captured accurately in this case. As a consequence, the turbulent flame brush is not captured accurately and a smaller spreading rate in the transverse direction is predicted by EBU, error that becomes more prominent further downstream.

Also, EBU tends to under-predict the centerline values by as much as 10%. It can be noted that the centerline region is also the region of low turbulent kinetic energy and EBU will predict here a reduced turbulent mixing rate. However, the experimental data show that the temperature maintains its high value over a large portion of the domain, so even with a reduced mixing rate the premixed reactants entrained in this region should burn at a high rate. The LEM model, on the other hand, avoids estimating the controlling rate and simulates the involved processes, thus allowing for a more accurate prediction of the temperature. The more accurate prediction of heat release results in more accurate spreading rates, which is reflected in the velocity field, as discussed earlier.

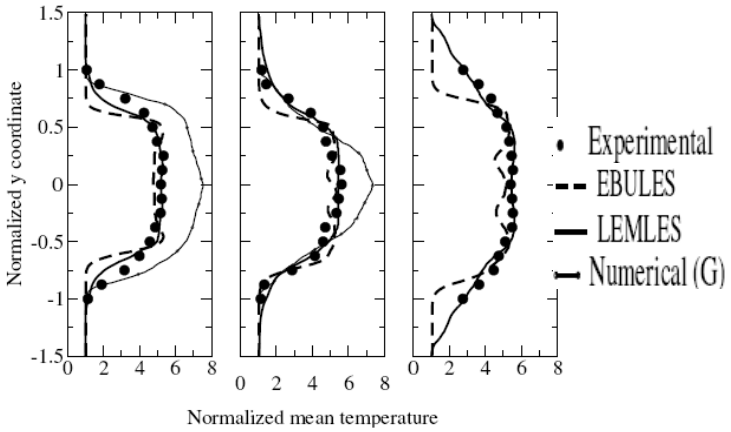

Fig. 8 – Transverse profiles of the normalized rms of the axial velocity fluctuation, at the normalized axial locations, from left to right: *0.375 a, 0.95 a, 1.53 a, 3.75 a* and *9.4 a*. The velocity is normalized by the inflow value, and the distance is normalized by the bluff body size, *a*.

These results demonstrate the subtle and global effects of using a more comprehensive combustion and mixing model as LEM. The significantly larger errors yielded

by the EDM numerical study [18] are probably due to insufficient grid resolution.

4.3 Turbulent fluctuations

The axial and the transverse velocity fluctuations along the transverse axis are presented, respectively in Figs. 9 and 10, together with previous experimental [68] and numerical [18, 69] data.

For the axial component, the EBU model tends to under-predict the velocity fluctuations at the centerline, while LEM predicts values in significantly better agreement with the experimental data due to the more accurate modeling of the flame - turbulence interaction. In the shear layer, the velocity fluctuations are generally over-predicted by both models, although the over-prediction decreases downstream, especially for LEM. The over-prediction by EBU is about twice as large in the near field when compared to LEM for both axial and transverse fluctuations.

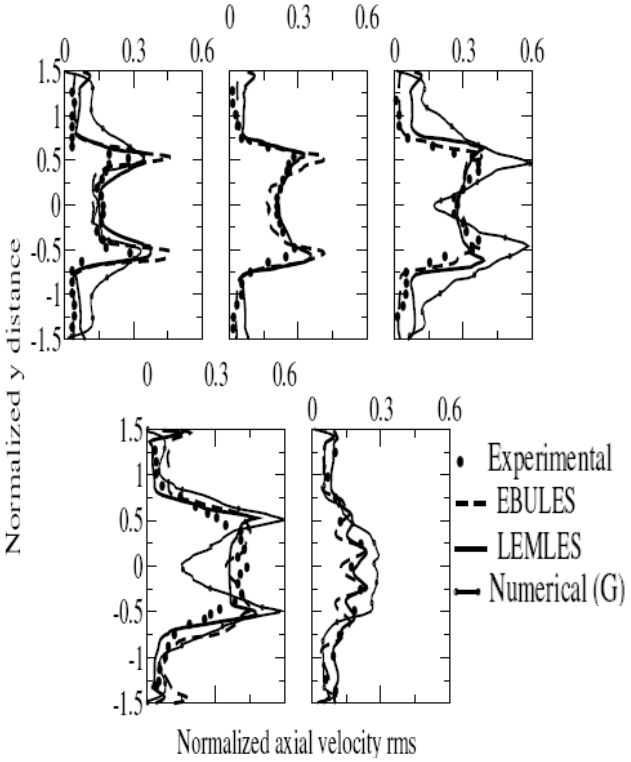

Fig. 9 – Transverse profiles of the normalized rms of the axial velocity fluctuation, at the normalized axial locations, from left to right: *0.375 a, 0.95 a, 1.53 a, 3.75 a* and *9.4 a*. The velocity is normalized by the inflow value, and the distance is normalized by the bluff body size, *a*.

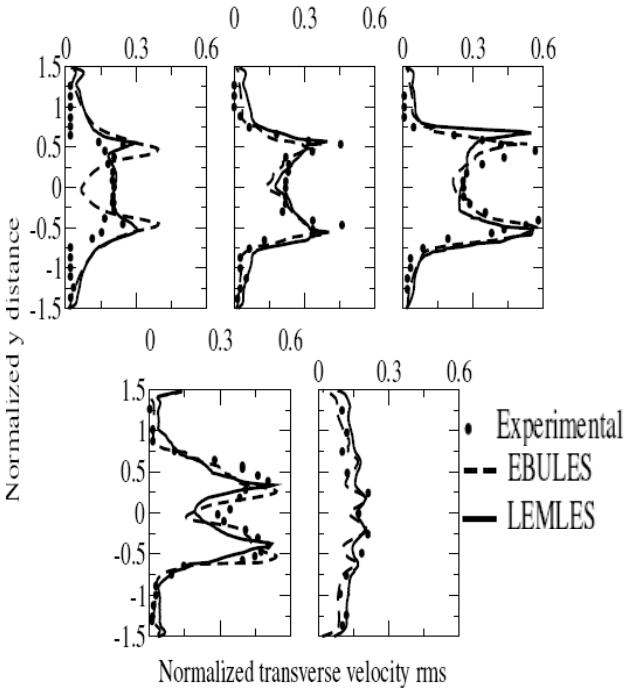

Fig. 10 – Transverse profiles of the normalized rms of the transverse velocity fluctuation, at the normalized axial locations, from left to right: *0.375 a, 0.95 a, 1.53 a, 3.75 a* and *9.4 a*. The velocity is normalized by the inflow value, and the distance is normalized by the bluff body size, *a*.

4 Conclusion

The main goal of this work was to develop and implement an efficient, highly scalable computational algorithm able to accurately capture the subtle features of a highly turbulent reactive flow. The best suited CFD method for this is a compressible LES approach. Although numerous such algorithms exist and have been successfully used in the past, this is, to the knowledge of the authors, the first such complex implementation on Romania and will be used by Romanian researchers to tackle complex turbulent combustion problems with state-of-the-art methods and computational tools.

The LES algorithm was validated by simulating a reactive flow behind a bluff body and by comparing the results against earlier experimental [68] and numerical data [18, 69]. The simulation results have shown the superiority of the LEM closure. On theoretical grounds, this was to be expected, since LEMLES needs no assumption about the decoupling between the turbulent scales and the combustion scales in the inertial range (the so-called "scale separation hypothesis" and, therefore, maintains its validity over the entire range of combustion regimes. Previous numerical simulations of similar geometries [2, 9, 18, 69, 70] have all failed to capture the correct experimentally measured spreading rate. A common feature of these studies was the laminar

chemistry assumption embedded in the combustion models (Eddy Dissipation Model [18, 70], or EBU [2, 9, 69]). As the simulated flame was proved to extend out of the validity range of the above mentioned combustion models, into the broken reaction zone regime [30], the flame thickness predicted by such models was over-predicted rendering the flame front less susceptible to turbulent fluctuations in the flow. Hence, flame surface wrinkling is significantly more pronounced in LEMLES, the flame structure is more complex, and the far field spreading of the wake is closer to the experimental observations. The time-averaged temperature in the low turbulence centerline region is underestimated by EBU, due to under-predicted turbulent mixing rates in the region. Consequently, the velocity fluctuations are also better predicted by the current study using LEM.

The current LEMLES implementation was proven to yield accurate results and is, therefore, suited for in-depth numerical studies of turbulent combustion. In combination with the LDKM model, the algorithm presented here has no adjustable ad-hoc parameters and is able to handle the entire range of combustion regimes and equivalence ratios.

References:

1 X. Bai, L. Fuchs, Modeling of turbulent reactive flows past a bluff body: Assessment of accuracy and efficiency. *Computers and Fluids*, Vol. 23, No. 3, 1994, pp. 507-521.

2. C. Fureby, S. I. Moller, Large eddy simulations of chemically reactive flows applied to bluff body stabilized flames, *AIAA Journal*, Vol. 33, No. 12, 1995, pp. 2339-2347.

3. M. Saghafian, P. K. Stansby, M. S. Saidi, D. D. Apsley, Simulation of turbulent flows around a circular cylinder using nonlinear eddy viscosity modeling: Steady and oscillatory ambient flows. *Journal of Fluids and Structures*, Vol 17, No. 8, 2003, pp.1213-1236.

4. F. Lien, E. Yee, Numerical modeling of the turbulent flow developing within and over a 3-d building array. part i: A high-resolution Reynolds-averaged Navier-Stokes approach, *Boundary-Layer Meteorology*, Vol. 112, No. 3, 2004, pp. 427-466.

5. A. Frendi, G. Skarath, A. Tosh, Prediction of noise radiated by flow over a smooth square cylinder, *10th AIAA/CEAS Aeroacoustics Conference*. Manchester, UK, 2004.

6. J. Smagorinsky, General circulation experiments with the primitive equations. I. The basic experiment, *Monthly Weather Review*, Vol. 91, No. 3, 1963, pp. 99-164.

7. D. K. Lilly, The representation of small-scale turbulence in numerical simulation experiments. *Proceedings of the IBM Scientific Symposium on Environmental Sciences*, IBM. Yorktown Heights, NY, 1967, pp. 195-210

8. J. W. Deardorff, Three-dimensional numerical study of the height and mean structure of a heated planetary boundary layer, *Boundary-Layer Meteorology*, Vol. 7, 1974, pp.81-106.

9. C. Fureby, C. Lofstrom. Large-eddy simulations of bluff - body stabilized flames, *Twenty- Fifth Symposium (International) on Combustion*, 1994, pp. 1257-1264.

10. C. Fureby, Large-eddy simulations of turbulent anisochoric flows, *AIAA Journal*, Vol. 33, No. 7, 1995, pp. 1263-1272.

11. C. Fureby, On sub grid scale modeling in large eddy simulations of compressible fluid flow, *Physics of Fluids*, Vol. 8, No. 5, 1996, pp. 1301-1311.

12. S. Moller, E. Lungren, C. Fureby. Large-eddy simulations of unsteady combustion, *Twenty - Fifth Symposium (International) on Combustion*, 1996, pp. 1257-1264.

13. C. Fureby, Large eddy simulation of combustion instabilities in a jet engine afterburner model, *Combustion Science and Technology*, Vol. 161, 2000, pp. 213-244.

14. C. Fureby, A computational study of combustion instabilities due to vortex shedding, *Proceedings of the Combustion Institute*, Vol. 28, 2000, pp. 783-791.

15. R. Ryden, L. Eriksson, S. Olovsson, Large eddy simulation of bluff body stabilized turbulent premixed flames, *International Gas Turbine and Aero - Engine Congress and Exposition*, ASME - 93 - GT - 157, 1993.

16. S. Inage, V. Perez, N. Kobayashi, An evaluation of premixed combustion around a bluff body using a combustion model, *JSME International Journal*. Series B, Vol. 41, No. 3, 1998, pp. 650-656.

17. V. K. Chakravarthy, *Stochastic Subgrid Modeling of Turbulent Premixed Flames*, PhD thesis, Georgia Institute of Technology, Atlanta, Georgia, USA, 2000.

18. E. Giacomazzi, V. Battaglia, C. Bruno, The coupling of turbulence and chemistry in a premixed bluff-body flame as studied by LES, *Combustion and Flame*, Vol. 138, 2004, pp. 320-335.

19. C. Stone, S. Menon, Parallel simulations of swirling turbulent flames, *Journal of Supercomputing*, Vol, 22, No. 1, 2002, pp. 7-28.

20. C. Stone, S. Menon. LES of partially-premixed unsteady combustion. *AIAA-2003-0316*, 2003.

21. C. Duwig, R. Z. Szasz, L. Fuchs, C. Troger, Large eddy simulation of a swirling flame response to swirl modulation with impact on combustion stability, *AIAA-2005-1275*, 2005.

22. P. Domingo, L. Vervisch, K. Bray, Partially premixed flamelets in LES of nonpremixed turbulent combustion, *Combustion Theory and Modelling*, Vol. 6, 2002, pp. 529-551.

23. B. Fiorina, O. Gicquel, L. Vervisch, S. Carpentier, N. Darabiha, Approximating the chemical structure of partially premixed and diffusion counterflow flames using FPI flamelet tabulation, *Combustion and Flame*, Vol. 140, 2005, pp. 147-160.
24. M. Dosing, A. Kempf, F. Flemming, A. Sadiki, J. Janicka, Combustion LES for premixed and diffusion flames, *Progress in Computational Fluid Dynamics*, Vol. 5, No. 7, 2005, pp. 363-374.
25. P. G. Mehta, M. C. Soteriou, Combustion heat release effects on the dynamics of bluff body stabilized premixed reacting flows, *AIAA-2003-0835*, 2003.
26. P. G. Mehta, A. Banaszuk, M. C. Soteriou, Impact of convection and diffusion in fundamental limitations of combustion control, *AIAA-2004-2410*, 2004.
27. R. R. Erikson, M. C. Soteriou, P. G. Mehta, The influence of temperature on the dynamics of bluff body stabilized flames, *AIAA-2006-0753*, 2006.
28. L. Vervisch, R. Hauguel, P. Domingo, Direct numerical simulation (DNS) of premixed turbulent V-flames, *AIAA-2003-4497*, 2003.
29. N. Peters, *Turbulent Combustion,* Cambridge University Press, Cambridge, U.K., 2000.
30. I. Porumbel, *LES of Bluff Body Stabilized Premixed and Partially Premixed Combustion* VDM Verlag Dr. Muller, Saarbrücken Germany, 2006
31. M. Germano, P. Piomelli, U. Moin, W. H. Cabot, A dynamic sub-grid scale eddy viscosity model, *Proceedings of the Summer Program*, 1990, pp 5-17, 1990.
32. P. Moin, W. Squires, W. Cabot, S. Lee, A dynamic sub-grid scale model for compressible turbulence and scalar transport, *Journal of Fluid Mechanics*, Vol. 3, No. 11, 1991, pp. 2746-2757.
33. G. Erlebacher, M. Y. Hussaini, C. G. Speziale, T. A. Zang, Toward the large eddy simulation of compressible turbulent flows, *Journal of Fluid Mechanics*, Vol. 238, 1992, pp. 155-185.
34. S. Menon, Active combustion control in a ramjet using large eddy simulations. *Combustion Science and Technology*, Vol. 84, 1992, pp. 51-79.
35. A. N. Kolmogorov, Local structure of turbulence in incompressible fluids with very high Reynolds number. *Dokl. Acad. Nauk*, Vol. 30, 1941, pp. 229.
36. S. Ghosal, On the large-eddy simulation of turbulent flows in complex geometries, *Technical report, Center for Turbulence Research*, 1993.
37. S. B. Pope, *Turbulent Flows,* Cambridge University Press, 2000.
38. U. Schumann, Subgrid scale model for finite difference simulations of turbulent flows in plane channels and annuli, *Journal of Computational Physics*, Vol. 18, 1975, pp. 376-404.
39. W. W. Kim, S. Menon. A new incompressible solver for large - eddy simulations, *International Journal of Numerical Methods in Fluids*, Vol. 31, 1999, pp. 983-1017.
40. W. W. Kim, S. Menon, H. C. Mongia. Large eddy simulation of a gas turbine combustor flow, *Combustion Science and Technology*, Vol. 143, 1999, pp. 25-62.
41. S. Menon, P. K. Yeung, W. W. Kim, Effect of subgrid models on the computed interscale energy transfer in isotropic turbulence, *Computers and Fluids*, Vol. 25, No. 2, 1996, pp. 165-180.
42. C. Fureby, *On Modeling of Unsteady Combustion Utilizing Continuum Mechanical Mixture Theories and Large Eddy Simulations,* PhD thesis, Lund Institute of Technology, Lund, Sweden, 1995.
43. D. Veynante, J. Piana, J. M. Duclos, C. Martel. Experimental analysis of flame surface density models for premixed turbulent combustion, *Twenty - Sixth Symposium (International) on Combustion*, 1996, pp. 1249-1256.
44. V. K. Chakravarthy, S. Menon, Linear - eddy simulations of Reynolds and Schmidt number dependencies in turbulent scalar mixing, *Physics of Fluids*, Vol. 13, 2001, pp. 488-499.
45. W.-W. Kim, S. Menon. A new dynamic one-equation subgrid-scale model for large-eddy simulations, *AIAA-95-0356*, 1995.
46. C. C. Nelson, S. Menon, Unsteady simulations of compressible spatial mixing layers, *AIAA - 98 - 0786*, 1998.
47. C. Fureby, N. Alin, N. Wikstrom, S. Menon, N. Svanstedt, L. Persson, On large eddy simulation of high Reynolds number wall bounded flows, *AIAA Journal*, Vol. 42, No. 3, 2004, pp. 457-469.
48. S. James, J. Zhu, M. Anand, Large-eddy simulations as a design tool for gas turbine combustion systems. *AIAA Journal*, Vol. 44, No. 4, 2006, pp. 674-686.
49. S. Kirpekar, D. Bogy, A benchmark for the flow across a square cylinder using commercial CFD codes, *APS Division of Fluid Dynamics 58th Annual Meeting*, November 2005, Chicago, IL.
50. A. R. Kerstein, Linear-eddy modeling of turbulent transport ii. *Combustion and Flame*, Vol. 75, 1989, pp. 397-413.
51. S. Menon, P. A. McMurtry, A. R. Kerstein, A linear eddy mixing model for large eddy simulation of turbulent combustion. *LES of Complex Engineering and Geophysical Flows,* Ed. B. Galperin and S. Orszag, 1993.
52. C. K. Westbrook, F. L. Dryer, Simplified reaction mechanisms for the oxidation of hydrocarbon fuels in flames, *Combustion Science and Technology*, Vol. 27, 1981, pp. 31-43.
53. V. Sankaran, I. Porumbel, S. Menon. Large-eddy simulation of a single-cup gas turbine combustor. *AIAA-2003-5083*, 2003.

54. T. M. Smith, S. Menon, One-dimensional simulations of freely propagating turbulent premixed flames, *Combustion Science and Technology*, Vol. 128, 1996, pp. :99-130.
55. V. K. Chakravarthy, S. Menon, Large - eddy simulations of turbulent premixed flames in the flamelet regime. *Combustion Science and Technology*, Vol. 162, pp. 1-48.
56. V. Chakravarthy, S. Menon, Subgrid modeling of premixed flames in the flamelet regime, *Flow, Turbulence and Combustion*, 2001a.
57. V. Sankaran, *Subgrid Combustion Modelling for Compressible Two - Phase Reacting Flows,* PhD thesis, Georgia Institute of Technology, Atlanta, Georgia, USA, 2002.
58. A. Jameson, W. Schmidt, E. Turkel, Numerical solutions of the Euler equations by finite volume methods with Runge Kutta time stepping schemes, *AIAA-81-1259*, 1981.
59. J. J. Alonso, A. Jameson, Fully - implicit time - marching aeroelastic solutions, *AIAA-94-0056*, 1994.
60. J. Yao, A. Jameson, J. J. Alonso, F. Liu. Development and validation of a massively parallel flow solver for turbomachinery flows, *Journal of Propulsion and Power*, Vol. 17, No. 3, 2001, pp. 659-668.
61. H. Lomax, P. Kutler, F. B. Fuller, *The Numerical Solution of Partial Differential Equations Governing Convection,* AGARDograph, 1970.
62. J. C. Tannehill, D. A. Anderson, R. H. Pletcher, *Computational Fluid Mechanics and Heat Transfer*, Taylor and Francis, 1997.
63. L. Martinelli, A. Jameson, Validation of a multigrid method for the Reynolds averaged equations, *AIAA-88-0414*, 1988.
64. A. Jameson, Time dependent calculations using multigrid, with applications to unsteady flows past airfoils and wings, *AIAA-91-1596*, 1991.
65. W. H. Calhoon, S. Menon, G. Goldin, Comparison of reduced and full chemical mechanisms for nonpremixed turbulent H_2 - air jet flames, *Combustion Science and Technology*, Vol. 104, 1995, pp. :115-141.
66. T. M. Smith, S. Menon, The structure of premixed flames in a spatially evolving turbulent flow. *Combustion Science and Technology*, Vol. 119, No. 1-6, 1996, pp. 77-106.
67. W. H. Calhoon, S. Menon, Subgrid modeling for reacting large eddy simulations, *AIAA-96-0516*, 1996.
68. A. Sjunesson, S. Olovsson, B. Sjoblom, Validation rig - a tool for flame studies, *Technical Report* 9370-3088, 1991.
69. I. Porumbel, S. Menon, Large-eddy simulation of bluff body stabilized flames, *AIAA-2006-0152*, 2006.
70. A. Sjunesson, R. Henriksson, C. Lofstrom, CARS measurements and visualization of reacting flows in bluff body stabilized flame, *AIAA - 92 - 3650*, 1992.